Detonation Propagation and Mach Stem Formation in PBXN-9

Lawrence M. Hull
Los Alamos National Laboratory

Abstract

PBXN-9 is an explosive that is less sensitive to certain insults, yet retains a high level of performance. As a result, PBXN-9 has been considered as an interim insensitive high explosive for conventional munitions systems. Certain of these systems incorporate wave control methodologies that require some form of reactive flow representation to achieve accurate predictions of the wave propagation. We have continued our use of Detonation Shock Dynamics (DSD) as a means to approximately account for reactive flow effects, yet retain the efficiency necessary for the munitions design process. To use DSD, we have taken the approach to calibrate explosives by measuring the detonation velocity as a function of local wave curvature. The DSD calibration, including the appropriate boundary conditions, can then be used to predict wave propagation in complex situations such as around obstacles, following wave-wave collisions, and so on. This paper describes the DSD calibration for PBXN-9, along with the methodologies used to obtain it, for both convergent and divergent flow (positive and negative wave curvatures). During the course of the calibration for convergent flow, Mach stem formation is observed in wave reflection experiments. The characteristics of the Mach stem formation and the subsequent growth are analyzed, presented and compared to similar measurements on other explosives. Illustrative examples of the use of DSD to predict wave propagation are provided.

Introduction

In the simplest form, the Detonation Shock Dynamics theory (Ref. 1, 2) can be reduced to a linear relationship between the normal detonation velocity and the local wave curvature. The linear relationship can be written as the Chapman-Jouguet (CJ) velocity modified by a curvature term,

$$D=Dj(1-\alpha\kappa), \qquad \text{Eq. (1)}$$

where κ is the curvature and α is a constant that contains information from the reaction zone. The theoretical approach proceeds by postulating a reaction rate law which, with the conservation equations and an equation of state that includes reaction progress, leads to the existence of a relationship between the curvature and the normal velocity. In the first order (linear) relation, the theory yields the unknown coefficient of the curvature in terms of an uncertain reaction description. Rather than attempt to measure or otherwise identify the correct reaction rate law, one can simply measure the velocity-curvature relation and proceed with applications. This is valid because the velocity-curvature relation is a material characteristic and is independent of the geometry.

The DSD detonation approach has now been implemented into hydrocodes (Ref. 3, 4), and a calibration is needed for each explosive to be used. To be useful in general, the calibration must span both negative and positive curvatures. Several explosives have been calibrated, and a few include the negative curvature region. PBXN-9 is an explosive that is less sensitive to certain insults, yet retains a high level of performance due to the high HMX content. This explosive is of current interest and is the primary topic of this paper. The experimental techniques used for the N-9 characterization correspond to those used for PBX-9502 and PBX-9501, Ref. (5,6). The positive curvature region is accessed by measuring the shape of a detonation wave as it arrives at the end of a rate stick, and the

DISCLAIMER

negative curvature region is accessed by observation of colliding spherical detonation waves. We concentrate here on the negative curvature region. Since PBXN-9 is very near ideal, the curvature effects are expected to be slight and possibly more important in the negative curvature region in some applications. The Mach stem growth rate measured in the spherical colliding wave experiments, in conjunction with other information, can be used to compare PBXN-9 to other explosives. Therefore, the definition of the Mach stem width used for this purpose is discussed in detail here, and a comparison given. The paper concludes with two examples of using the DSD model in an Eularian hydrocode. The first example is to simply use the hydrocode to calculate the convergent calibration experiment. This is illustrative and constitutes a check on consistency. The second example is the dual end initiation of a copper tube filled with explosive, where the interest is focused on the response of the metal to interacting detonation waves.

Convergent Calibration

Interacting spherical detonation waves can be generated approximately by dual point initiation of explosive. Experiments of this type are used in the example problem and in the negative curvature calibration. During the analysis of the experimental data, an analytical approximation to the interacting spheres is used to allow estimation of the features of interest in the flow. The analytical approximation involves parameters that are determined through a curve fitting procedure. The curve fitting procedure is the same as that described in Ref. (5), with the exception of the Mach stem width definition. The geometry and the coordinate system used here is shown in Fig. 1. The smear camera records a normal view of the angled top of the explosive through a multiple slit pattern aligned such that the slits are parallel to the line through the initiation points. The smear camera records the arrival time of the wave as a function of transverse position at several distances from the origin. The purpose of the analysis is to reconstruct, at least approximately, the shape of the wave as it progresses through the explosive. From a time resolved representation of the wave interaction, we can estimate Mach stem width and growth rate, critical angle for stem formation, and detonation velocity-curvature relations. Consideration leads to the following observation: if the flow were to take place in an explosive of infinite extent (explosive fills the coordinate space) and is otherwise perfect (exactly placed detonators fired exactly at the same time, and are infinitely small points, etc.), then the wave would be rotationally symmetric around the line through the detonators. This is an idealized geometry because the boundary condition at the detonators is different and because the sides of the actual charge are cylindrical rather than flat. In the idealized case, it is seen that $y = 0$ is a plane of reflection. Observations of arrival time made on any plane will capture the evolution of the wave. We have elected to use a plane parallel to the y axis for convenience in the analysis. Figure 2 shows the idealized geometric construction in y-z plane, and defines the variables used in the analysis.

The smear camera record for Shot No. H1903 (PBXN-9) is given in Fig. 3. The camera records the self-light of the detonation wave. As the wave approaches the explosive surface, the light from the detonation is captured by the camera. A layer of water or mineral oil on the observation surface of the explosive quenches the light when the detonation arrives at the interface. The analysis of the record proceeds as follows.

We used ordinary photographic film as the recording medium. The negative was digitized with a high-quality scanner and the image is preprocessed to develop a low-noise derivative image. As implied above, the edge of interest is the late time edge on each self-light trace. Therefore, the image is arranged so that differentiation results in a minimum at the late time edge of each trace. Each slit trace on the derivative image is analyzed to extract the edge loci. Overlaying the extracted edges with the original image (the image without any preprocessing) is then be used to check for accuracy, Fig. 4. The expanded view of a portion of one slit shows that the extracted points are at the late time edge of the trace.

The static (taken through the smear camera just before the shot is fired) is used to obtain the magnification between the shot surface and the film plane. This gives the

transverse (along the slit) position information. Additionally, the lines probed by the slits are located from the magnification and readings of the slit positions. The time coordinate is generated by using the known writing speed once the pixel spacing in the time direction has been converted to mm on the film. Also, the slit spacing on the film produces an apparent time difference that must be removed. The extracted traces are shown in physical coordinates in Fig. 5.

The effective location of the initiation points, $(x_0, \pm y_0, z_0)$, is found from fitting the data that corresponds to the spherically expanding part of the waves (remove the data near the edges of the explosive and that in the irregular reflection region) to the equation of a sphere with radius expanding at the detonation velocity. For each trace, the line probed by the slit x = a, z = c is are known from the shot geometry, so we have

$$r^2 = (a - x_0)^2 + (|y| - y_0)^2 + (c - z_0)^2 \qquad \text{Eq. (2)}$$

and the radius is obtained from integration of Eq. (1). Consideration of the plane y = 0 results is the expression for the radius from the line through the detonators to the location of the Mach stem when it arrives at the slit,

$$r_m^2 = (a - x_0)^2 + (c - z_0)^2 \ . \qquad \text{Eq. (3)}$$

To obtain the Mach stem velocity the arrival of the Mach stem is taken to be the maximum arrival time for a each slit. Then, $D \approx \Delta r_m/\Delta t$, where the differences are from slit to slit so that the velocity applies midway between the slits. Interpolation is then used the get the measurement of D *at* the slit.

The radius of curvature, r_s, of the Mach stem is found by local analysis of that part of the arrival time data. The stem is taken to be a circle, moving at the velocity estimated above, that sweeps across the slit. The equation is, thus

$$r_s^2 = D^2(t - t_{s0})^2 + (y - y_{s0})^2$$

and the parameters of this fit are r_s, t_{s0}, and y_{s0}. Note that the origin is of no real interest and D is the Mach stem velocity.

This concludes the curve fitting process to obtain an analytic representation of the wave propagation. It provides the two principal radii of curvature and the velocity of the Mach stem surface and the effective location of the initiation points.

Once the curve fitting is complete, other items of interest can be calculated. By inspection, the mean curvature of the surface along the plane y = 0 (the saddle) is seen to be $\kappa = (1/r_m - 1/r_s)/2$. The normal detonation velocity of the Mach stem at each was a result of the curve fitting process. Therefore, the detonation velocity-curvature calibration for convergent flow is determined. The resulting calibration curve is given in Fig. 6, where it is also compared to those for PBX-9501 and PBX-9502. The straight line calibration for PBXN-9 is given by $D_n = 8.559(1 - 0.7948\ \kappa)$, where κ is the mean curvature in mm^{-1}.

Another item of interest is the Mach stem width. The most palatable definition is the location of the intersection of the reflected wave in the products with the incident wave. At best, this is difficult to detect with the camera technique used and, for some flows, the shock may connect over a region rather than at a simple point. Another definition is to detect the inflection point in the incident detonation wave. However, measurement of the inflection point can be noisy. A particularly simple approach is to define a Mach stem width as the chord half-length obtained from the condition that the torus (circle) that analytically represents the Mach stem osculates the expanding sphere at the moment the

stem arrives at the centerline. This definition allows for the derivation of analytic expressions for the interaction angle and Mach stem width in terms of the parameters achieved through the curve fitting process.

The derivation is based on the assumption that the geometry is a figure of revolution, Fig. 2. To derive the equations, define the vector **E** to have the center of the stem torus as the end point and the intersection of the rotation axis with the plane y = 0, $(x_0, 0, z_0)$, as the starting point. Also define **F** to have the same end point, but start at (x_0, y_0, z_0) (the effective detonator location). In the plane defined by **E** and **F**, we can see the following relations:

$$\mathbf{F} = \mathbf{E} - y_0\mathbf{j} \text{ and } \mathbf{E}\bullet\mathbf{F}=EF\sin\alpha$$

where α is the interaction angle. Since **E** has no j component, we get

$$\mathbf{E}\bullet\mathbf{F}=E^2$$

and the first relation gives

$$\mathbf{F}\bullet\mathbf{F}=F^2 = E^2 + y_0^2 \ .$$

Further, the magnitude of E, in terms of the fitted parameters, must be $r_m + r_s$ to meet the osculation condition. Combining all of these give the interaction angle as

$$\sin\alpha = \frac{E}{F} = \frac{1}{\sqrt{1+\left(\frac{y_0}{r_m + r_s}\right)^2}}$$

Also from Fig. 2, we have

$$w = r_s \cos\alpha \, .$$

Eliminating α gives:

$$\frac{w}{r_s} = \frac{1}{\sqrt{1+\left(\frac{1+r_s/r_m}{y_0/r_m}\right)^2}}$$

The limits of this expression for w are physically acceptable. As the Mach stem just forms, $r_S \rightarrow 0$ and the relation gives $w \rightarrow 0$. As the wave runs indefinitely, $r_S \rightarrow \infty$, and the relation gives $w \rightarrow y_0$.

Fig. 7 provides a comparison of the Mach stem widths defined as above for PBXN-9, PBX-9501, and PBX-9502. The comparison shows that the Mach stem grows about the same in N-9 as in 9501. This result is consistent with the fact that N-9 is a high HMX content explosive. As seen in Fig. 7, Mach stems grow much faster in PBX-9502, a result consistent with the relatively large reaction zone of PBX-9502.

Divergent Flow Data

A 10 mm diameter rate stick of N-9 was fired to obtain data on the divergent portion of the velocity calibration. A steady detonation wave is allowed to develop and then the

detonation velocity is measured using pins and curvature is measured using a smear camera. Nominally, this technique accesses in a relatively large portion of the divergent velocity-curvature relation because the center of the stick is near $\kappa=0$ and the edges are at larger κ because of the free surface release. To obtain unambiguous results, the wave must be steady and symmetric, and we must be able to record front curvature data right up to the edge of the stick. A small stick diameter induces more variation in curvature and therefore helps to extend the range of the data. Therefore, we chose to make a stick 10 mm in diameter and 150 mm long.

The front curvature measurement technique consists of reflecting light from the surface of the mirror into the camera, Ref(6). The mirror is glued on to the front of the stick onto a surface machined on an angle inclined with respect to the axis of the stick. When the lead shock of the detonation wave arrives, the mirror is turned and the light is directed out of the camera. The camera record obtained in Shot H1885 is shown in Fig. 8. Analysis results in one or more points in the positive curvature region.

Examples of Applications

As mentioned in the introduction, the first example given here is the use of the DSD model in an Eularian hydrocode to simply calculate the convergent calibration experiment for PBXN-9. This is illustrative and constitutes a check on consistency. The problem is set up using the geometry in Fig. 2. The coordinate system is cylindrical with the z-axis taken to be the line between the two effective initiation points. The total explosive thickness in the z-direction is 100 mm, the same as the calibration charge. As described above, this geometry approximates the actual calibration experiment. To compare the results calculated to the smear camera data, marker particles were placed in each cell along a line that corresponds to the line probed by the camera. The arrival time of the first shock is recorded by the marker particles and compared to the camera data. The calculational cells are 0.5 mm x 0.5 mm. The straight line calibration curve given in Fig. 7 was used along with the JWL equation of state for PBXN-9 and the appropriate boundary conditions (which involves the unreacted Hugoniot, Ref. 2, 3).

Two calculations were run. The set-up was identical for each except that the DSD model was used in one and the ordinary programmed burn (Huygen's construction) was used in the other. The results are compared to the data captured in Shot H1903 in Figures 9 and 10. In Fig. 9, the calculation is compared to the trace identified as "0" in Figs. 3 and 5. The programmed burn calculation gives a cusp where the waves intersect and the DSD calculation gives the irregular reflection configuration as seen in the data. The same remark holds for the comparison given in Fig. 10 for trace 3.

The second example is the dual end initiation of a copper tube filled with explosive. The initial configuration is shown in Fig. 11 and radiographic data, Ref. (7) from one such experiment is shown in Fig. 12. The cylinder of explosive inside the copper tube is detonated at opposite ends. The detonations propagate down the charge and collide at the center. As the detonation wave first sweeps along the tube wall, the tube expands as in a normal cylinder test. However, when the waves collide in the center, the interaction that occurs cuts through the tube wall. The radiograph shown in Fig. 12 was taken long after the wave collision, and the cutting is obvious. It should be noted that in this particular problem, the wave interaction would likely form a regular reflection rather than a Mach reflection. As a result, it might be expected that the programmed burn approximation would give the same results as the DSD approximation (because the Mach stem generated by the DSD approximation should be very small).

The calculations of this geometry were carried out in much the same fashion as those of the first example. The cell size was 0.2 mm by 0.2 mm. Again two cases were run to contrast the DSD calculation and the programmed burn calculation. In Fig. 13, a pressure contour plot shows the dual point detonation before collision. In Fig. 14, the wave interaction in the explosive has driven the a similar wave interaction into the copper.

Many of the parameters provided by the DSD method of wave propagation influence the conditions driven into the copper. The velocity of the detonation and the angle of the detonation waves both before and after they have collided are important as is the pressure in the explosive products behind the wave interaction. Further, the angle the detonation wave makes with the copper wall will also influence the flow.

The differences between the DSD calculation and the programmed burn calculation are not apparent in large scale contour plots. Therefore, the pressure was monitored by marker particles in the copper along a line through the interaction parallel to the axis of the tube. In Fig. 15, the pressure histories are plotted for the particles used in the DSD calculation. The second compression associated with the wave reflection is obvious. In Fig. 16, the peak pressure recorded by each marker particle is plotted as a function of initial particle position to compare the DSD calculation to the programmed burn calculation. As can be seen, the distributions are quite similar, but the pressure is higher in the programmed burn calculation by about 50 kbar. This might be explained by the use of the plane wave (CJ) velocity in the programmed burn calculation. In the DSD calculation, the detonation velocity before the wave collision is less than the CJ velocity because the wave is divergent. Programmed burn ignores the divergence and uses the CJ velocity. Thus, in the programmed burn calculation, the velocity of the shock induced in the copper is higher, and so a correspondingly higher pressure is generated. It is quite clear that a consistent equation of state must be used with the DSD velocity-curvature relation. However, the equation of state to use for a programmed burn calculation may not be the best equation of state to use for a DSD calculation. There are other questions that arise from these preliminary calculations. From the original contour plots, it is clear that the cell resolution is course in the wave reflection region. Further studies must include mesh resolution studies as well studies of the influence of the DSD boundary and initial conditions.

References

1) D. S. Stewart and J. B. Bdzil, *Combust. Flame* **72**, 311 (1988).

2) J. B. Bdzil and D. S. Stewart, *Phys. Fluids A* **1**, 1261 (1989).

3) T. D. Aslam, J. B. Bdzil, and D. S. Stewart, *J. Comput. Phys.* **126**, 390-409 (1996).

4) At Los Alamos: Bdzil, Henninger, and Aslam implemented the level set approach described in Aslam, Bdzil, and Stewart (Ref. 3).

5) L. M. Hull, *10th Det. Symp.*, #97.

6) J. B. Bdzil, W. C. Davis, R. R. Critchfield, *Phys. of Fluids*, submitted.

7) Unpublished data, Lee, Ferm and Hull, Los Alamos, 1997.

Acknowledgments

This work was sponsored by the US Air Force and the Joint DoD/DOE Munitions Technology Program. Many personnel were involved in the entire scope of work that contributed to the results presented here. The many lively discussions with Eric Ferm, John Bdzil and Scott Stewart were critical to the completion of the work. The attention to precision and other details by George Chandler, John Horne, and Ron Boat resulted in the high-quality data collected in the PBXN-9 calibration experiments. My apologies to any others I have failed to acknowledge.

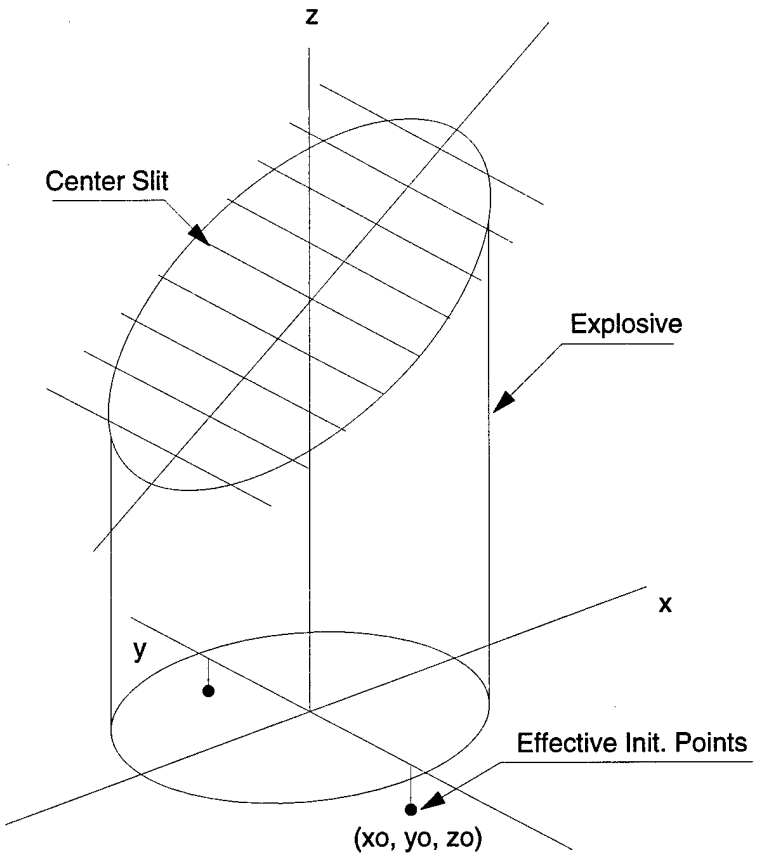

Fig. 1. Schematic of the dual point calibration experiment.

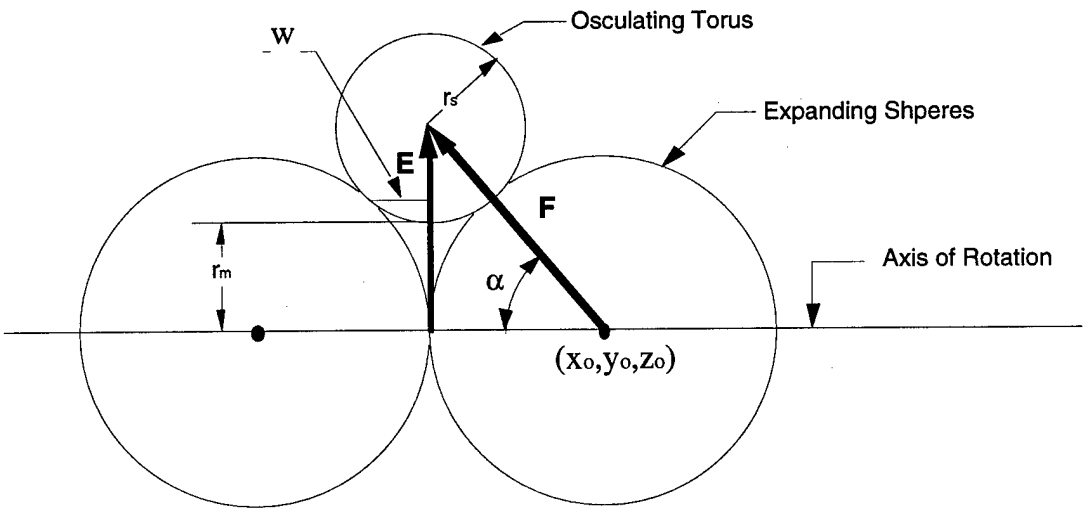

Fig. 2. The idealized wave interaction geometry (envision the y-z plane of Fig. 1).

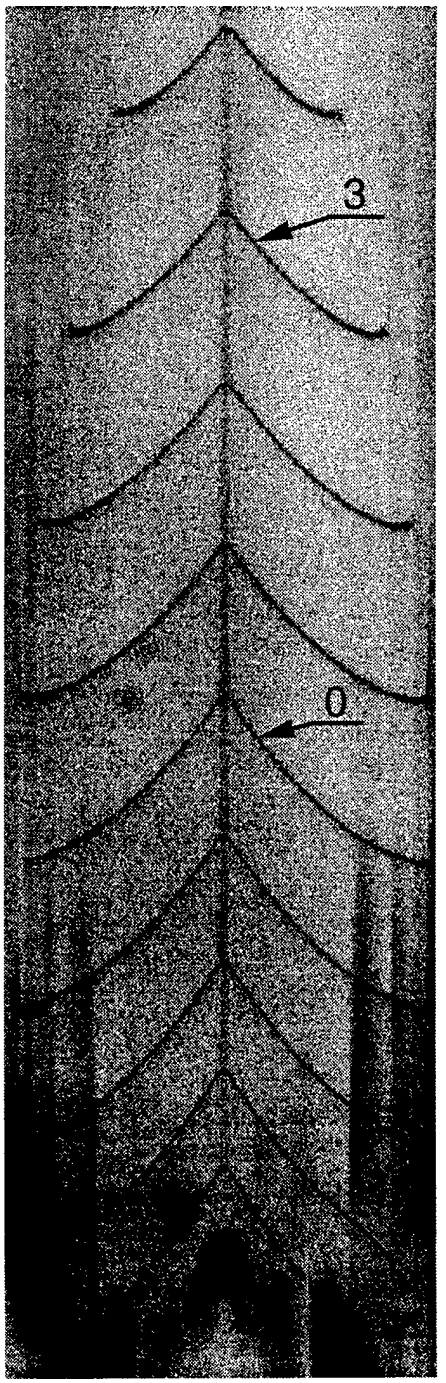

Fig. 3. The original smear camera record. Time increases upward. The traces used for comparisons are labeled with the trace from the center slit numbered 0.

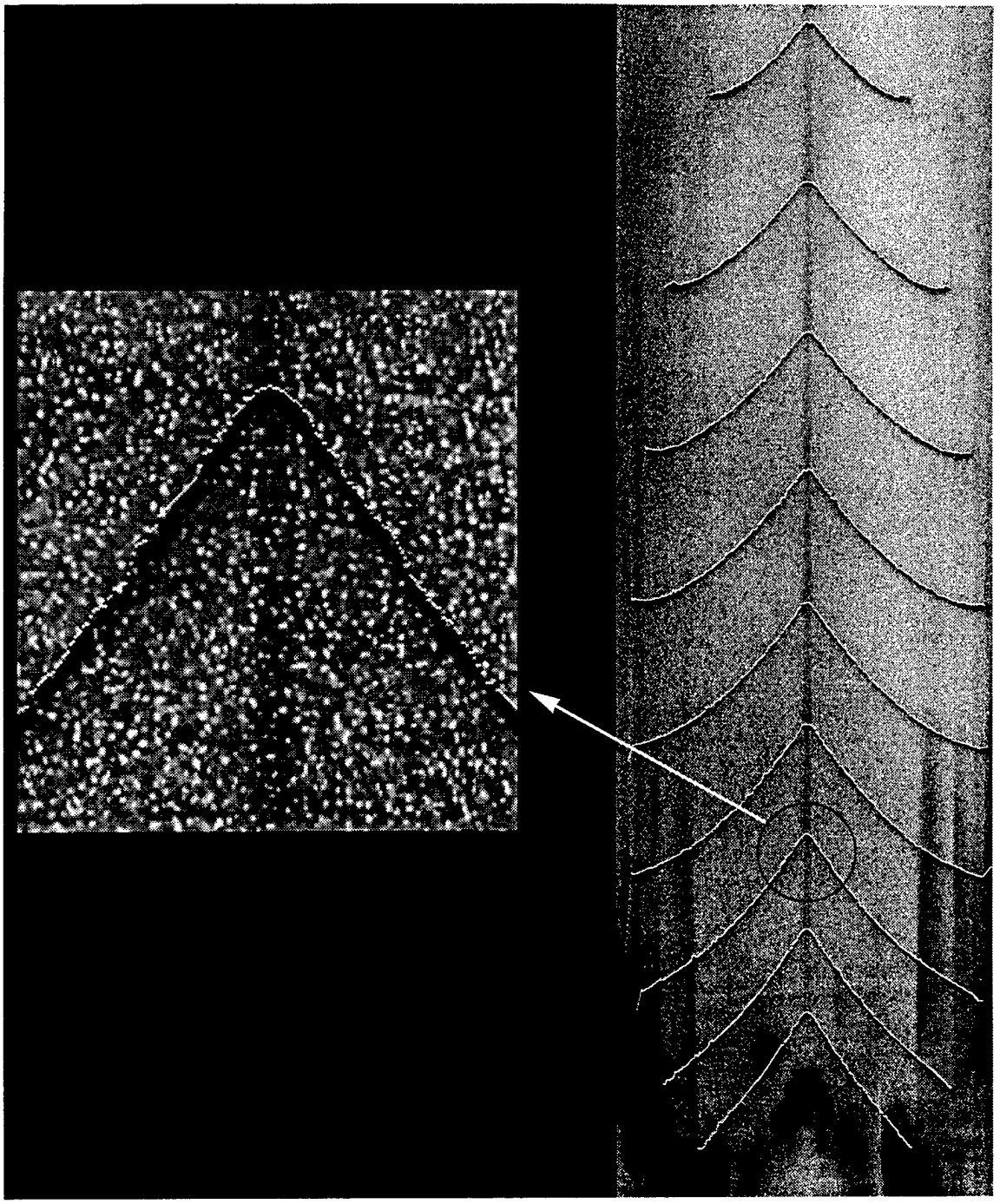

Fig. 4. Overlay of extracted arrival time data with the original camera record. The expanded view shows that the analysis extracts the late time edge of the trace.

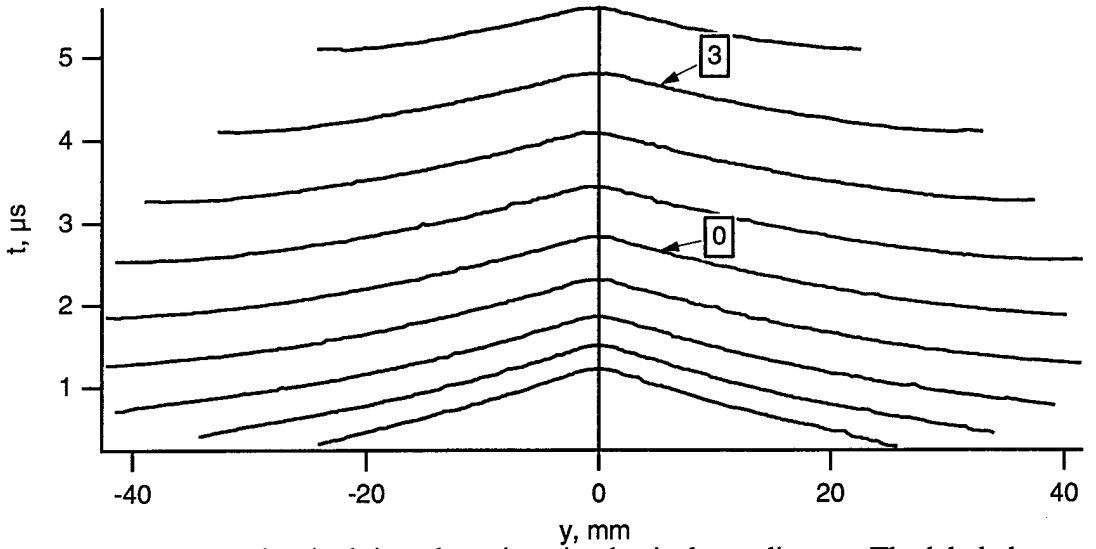

Fig. 5. The extracted arrival time data given in physical coordinates. The labeled traces correspond to those given in Fig. 3.

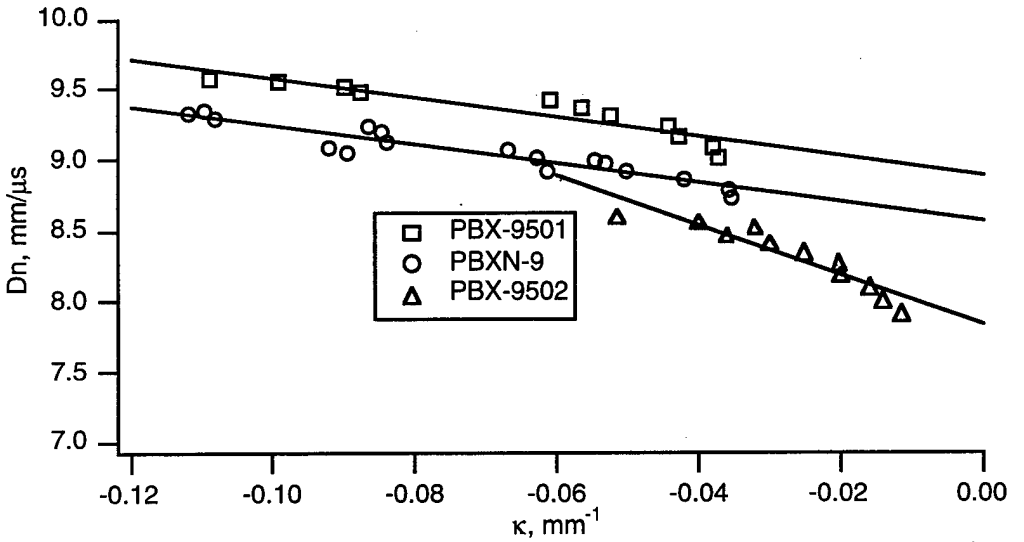

Fig. 6. The calibration curves for PBXN-9 compared to PBX-9501 and PBX-9502 (taken from Ref. (5).

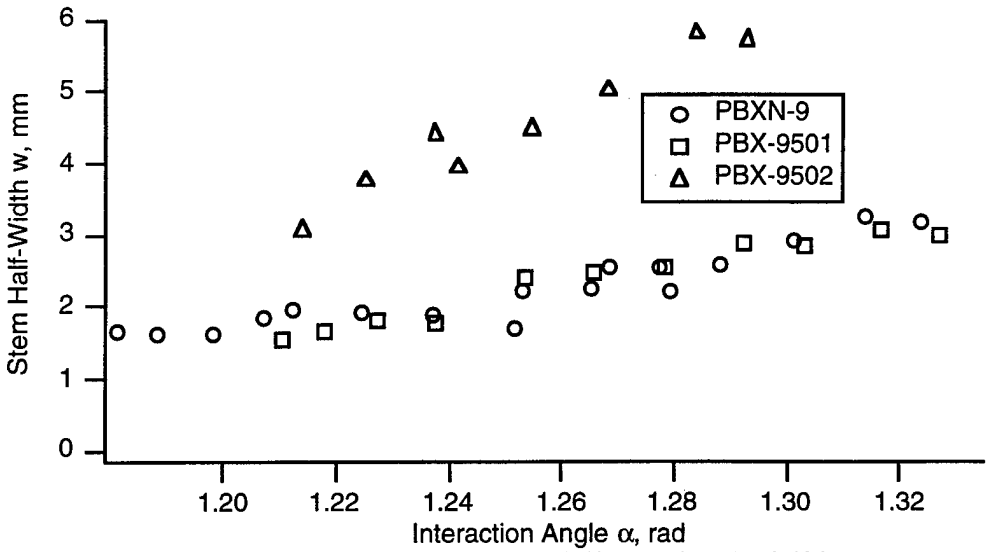

Fig. 7. Mach stem growth for PBXN-9, PBX-9501, and PBX-9502.

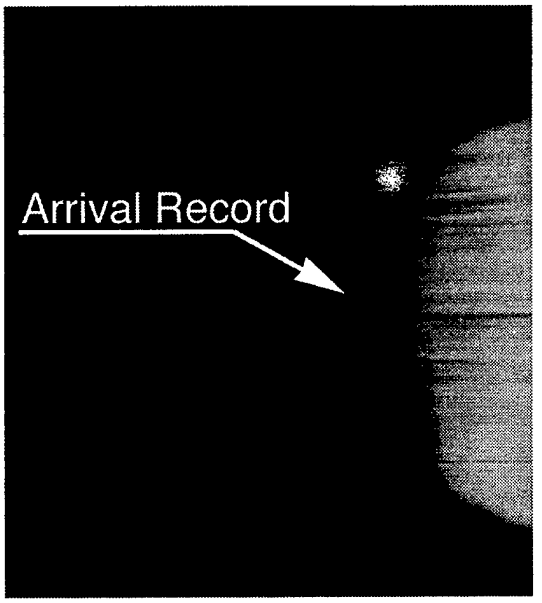

Fig. 8. Front curvature measurement on a PBXN-9 rate stick. Time increases to the right.

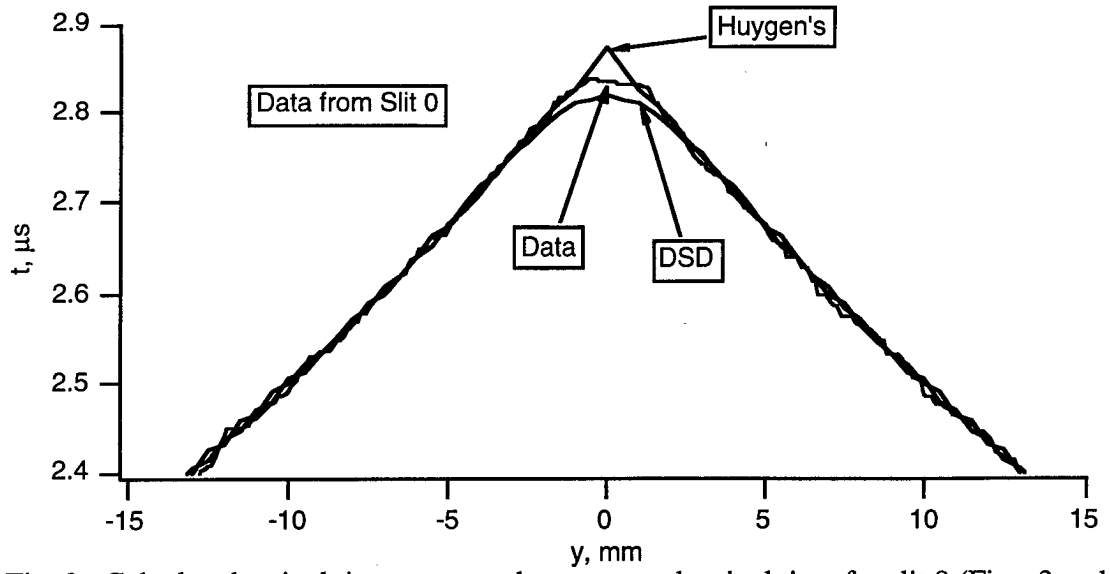

Fig. 9. Calculated arrival time compared to measured arrival time for slit 0 (Figs. 3 and 5).

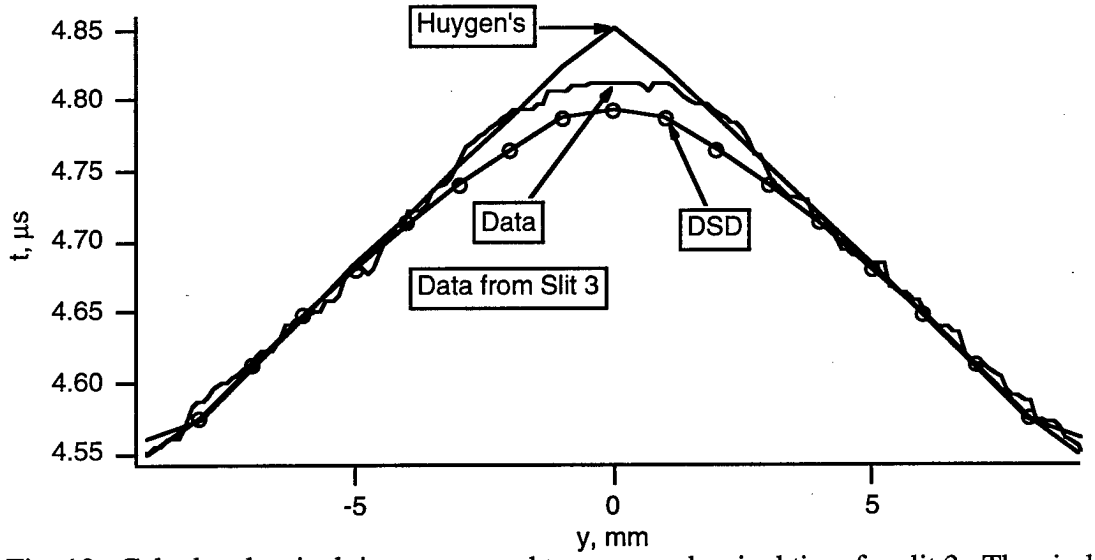

Fig. 10. Calculated arrival time compared to measured arrival time for slit 3. The circles indicate calculational cell centers.

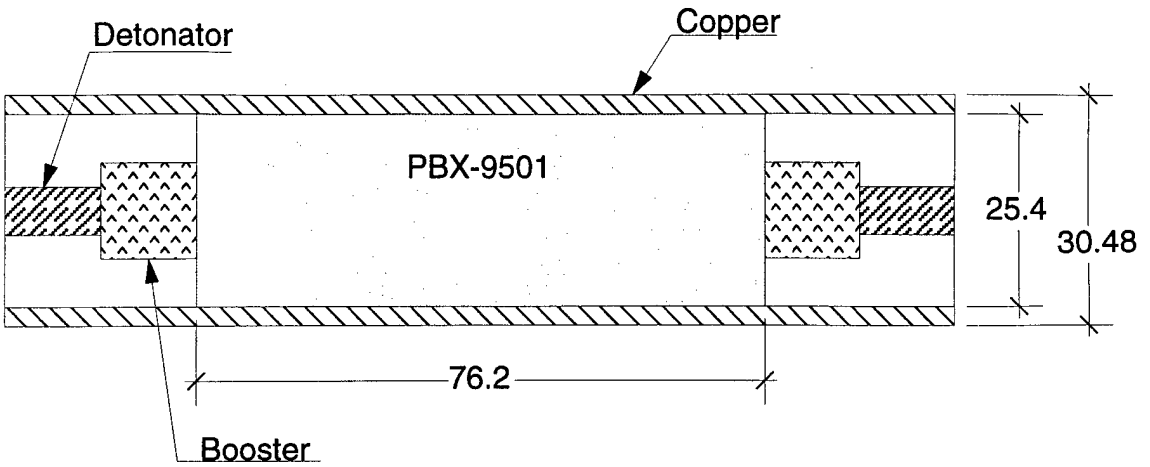

Fig. 11. Schematic of the copper tube wave interaction experiment.

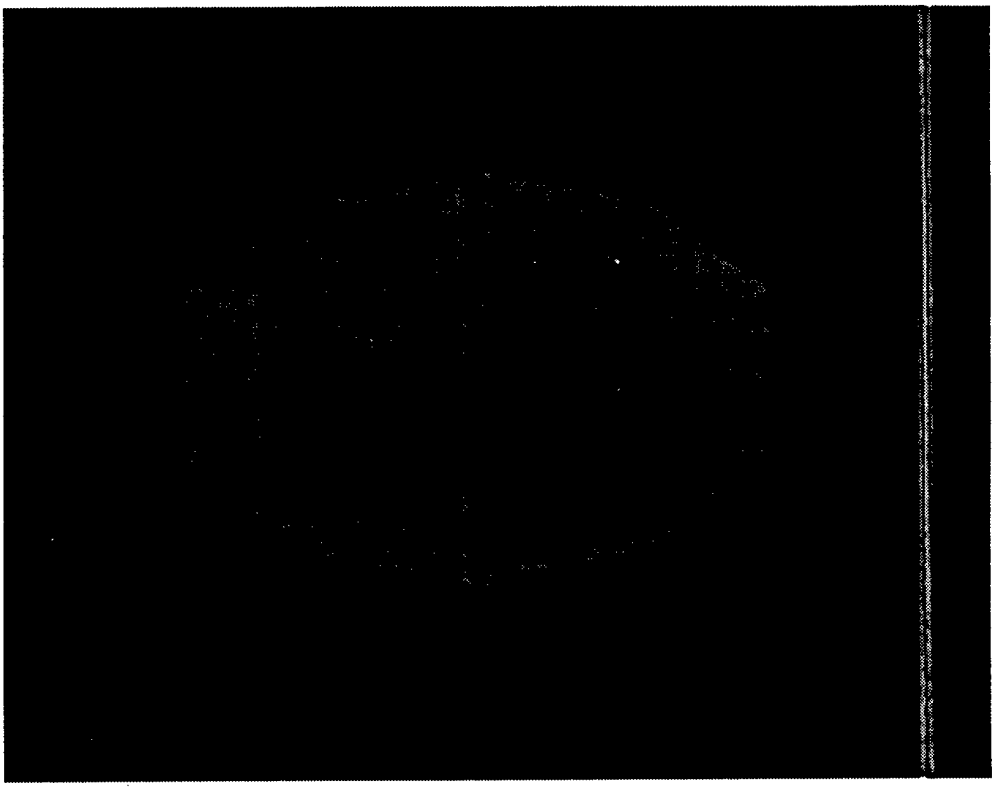

Fig. 12. Late time radiograph of the copper tube. Cutting or fracture is indicated by the dark line across the center of the tube.

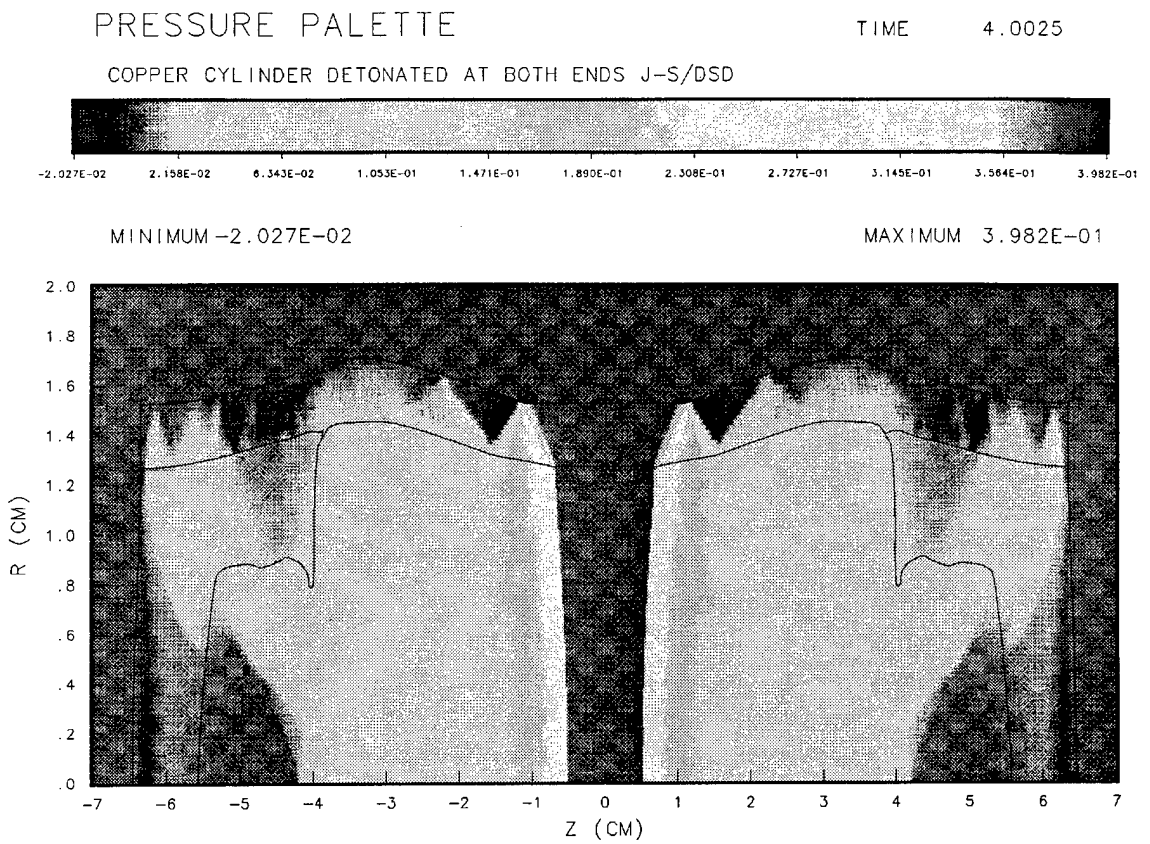

Fig. 13. Pressure contours of the dual end initiated copper tube calculation before wave collision.

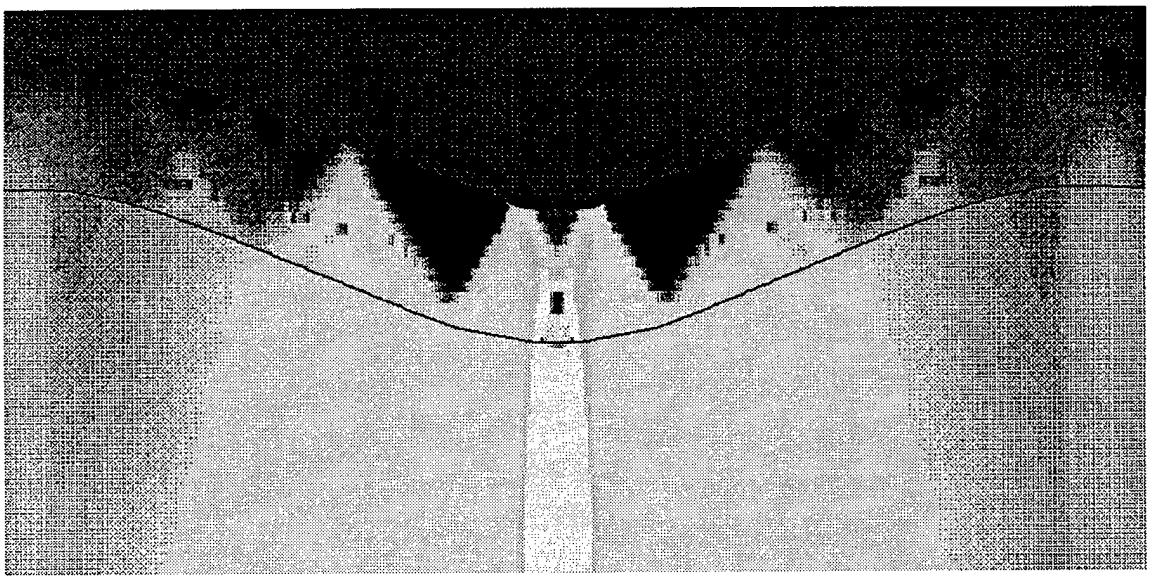

Fig. 14. Pressure contours of the dual end initiated copper tube, at 5 μs, while the wave interaction is propogating through the wall of the copper tube.

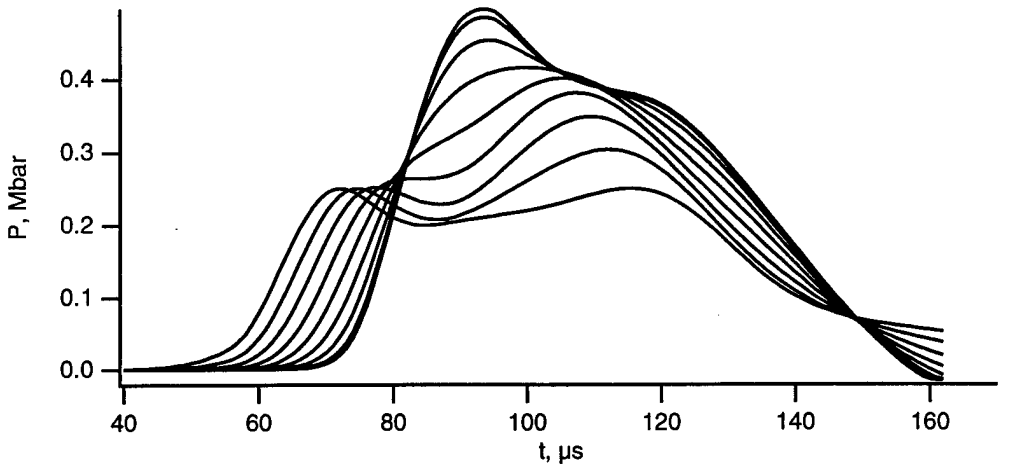

Fig. 15. Pressure histories of marker particles in the copper tube wall in the dual end initiated experiment.

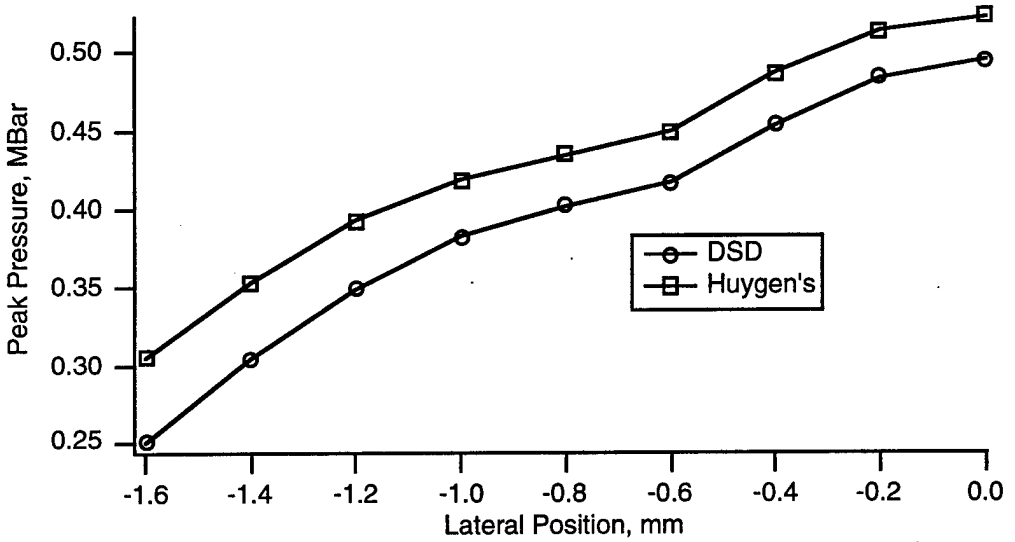

Fig. 16. Peak pressure of marker particles in the dual end initiated copper tube experiment plotted as a function of the initial particle position. The center of the tube, where the wave interaction occurs and the tube is cut, is at a lateral position of 0.

Report Number (14) LA-UR--97-3827
CONF-9709157--

Publ. Date (11) 199709
Sponsor Code (18) USAF; DOE/DP, XF
UC Category (19) UC-000; UC-741, DOE/ER

DOE